On the thermofluidics of a steady laminar jet impacting on a rotating hot plate: An *ab initio* scaling perspective

Cite as: AIP Advances **12**, 085311 (2022); https://doi.org/10.1063/5.0105060
Submitted: 22 June 2022 • Accepted: 25 July 2022 • Published Online: 17 August 2022

Durbar Roy and Saptarshi Basu

On the thermofluidics of a steady laminar jet impacting on a rotating hot plate: An *ab initio* scaling perspective

Cite as: AIP Advances 12, 085311 (2022); doi: 10.1063/5.0105060
Submitted: 22 June 2022 • Accepted: 25 July 2022 •
Published Online: 17 August 2022

Durbar Roy and Saptarshi Basu[a)]

AFFILIATIONS

Department of Mechanical Engineering, Indian Institute of Science, Bengaluru, KA 560012, India

[a)]Author to whom correspondence should be addressed: sbasu@iisc.ac.in

ABSTRACT

We provide an *ab initio* scaling analysis for liquid film thickness and Nusselt number of a steady laminar jet impinging a rotating heated plate. We have probed the limiting scaling regimes by incorporating the evaporative effects at the liquid–vapor interface. The dependence of liquid film thickness and Nusselt number on Reynolds, Rossby, and Prandtl numbers has been unearthed using scaling analysis of the integral and differential form of the continuity, Navier–Stokes, and energy equation in a cylindrical coordinate system. Boundary layer analysis has been used to discover a critical length that plays a significant role in understanding the effect of evaporation on hydrodynamic, thermal boundary layer thicknesses, and subsequently Nusselt number. The evaporative effects on liquid film thickness become increasingly important after a certain critical radius. The scaling laws derived are compared with existing experimental data available in the literature, and the trends predicted were consistent.

I. INTRODUCTION

Many scientists and engineers have pursued the hydrodynamics and heat transfer of liquid jet impinging a rotating heated plate in the past.[1–4] Liquid jets find much interest among the community due to their applications in various heat transfer devices such as radiators and evaporators in aerospace applications where efficiency is of utmost importance. Jets are considered effective in transferring heat and mass due to thin hydrodynamic and thermal boundary layer effects.[5,6] Cooling of electronic devices using high-speed jets is a highly effective technique used in the electronic and computing industries.[7–10] A lot of literature available considers a variety of conditions such as the effect of rotation, wall temperature, surface tension, to name a few[11] on heat transfer dynamics. Researchers have also analyzed liquid film thickness, Nusselt number, and hydraulic jump using experimental, numerical, semi-analytical, and analytical techniques.[12] Turbulent flow computations using the k–ε model in thin liquid fluid layers involving a hydraulic jump were accomplished by a group led by Rahman.[13] Rahman *et al.* worked out the numerical solutions of the momentum equations using finite difference techniques incorporating a boundary-fitted coordinate technique. Rahman and Faghri also carried out detailed works on rotating plates using a three-dimensional boundary-fitted coordinate system.[14] They concluded the dominance of inertia at the jet's entrance and rotation at the outer edge of the plate. Micro-gravity experiments and numerical simulations using potential flow theory were performed for free circular jets impinging on flat plates by scientists at NASA.[15] Avedisan and Zhao also studied circular hydraulic jumps in low gravity environments.[16] Heat transfer characteristics were calculated using integral analysis techniques by Liu and Lienhard.[17] They performed the computations for a uniform heated surface without rotations and discussed the effect of the Prandtl number on the Nusselt number. Rao and Arakeri studied free liquid jets using semi-analytical techniques such as the work of Liu and Lienhard.[18] Rao *et al.* used an integral analysis for the boundary layer equations using third-order polynomial approximations for the velocity profiles. Basu and Cetegen[19] studied the heat transfer analysis for jets impacting on rotating plates. They used integral analysis techniques to calculate the liquid film thickness and Nusselt number. Later work by the same group also focused on

hydraulic jumps.[20] Azuma and Hoshino studied the transition from laminar to turbulent, performed stability analysis, calculated liquid film thickness, and wall pressure fluctuations for the stationary horizontal plate.[21] The heat transfer characteristics, including Nusselt number calculations, were first studied by Chaudhury and group.[22] They developed closed-form solutions in the region where similarity solution exists. The heat transfer at the boundary between the liquid film and solid plate was solved separately, and then, the solutions were matched at the boundary by Wang and his colleagues.[23] The convective heat transfer from a jet of cooling oil to an approximately isothermal rotating plate was calculated by Carper and Deffenbaugh.[24] A later study by the same group incorporated the Prandtl number in the heat transfer characteristics. They provided many correlations from experimental data fitting. The numerous correlations developed in the literature[25] lacked fundamental physical and mathematical insights from first principles. Recently, different configurations of the fundamental jet impingement problem and the associated hydraulic jump dynamics have also been investigated experimentally, theoretically, and numerically.[26–28] Sen *et al.*[29] considered orthogonal liquid jet impingement on patterned surfaces of differential wettability (a surface having a combination of hydrophilic and hydrophobic patches). They found that the thin liquid film expands and breaks into droplets after a certain minimum liquid film thickness on a superhydrophobic surface. Benilov studied free surface flows down an inclined surface with slight inclinations theoretically.[30] A general set of asymptotic equations were derived to investigate hydraulic jumps and included lubrication and shallow water approximations as a limiting case. Wang *et al.* investigated the hydrodynamics and heat transfer of an axisymmetric liquid jet impinging a stationary circular plate heated from below.[31,32] They studied the effect of inertia, shear stress, wall heat flux, and wall temperature on the hydrodynamic and thermal boundary layer. Some new results relating to the hydraulic jump in normal impinging jets were reported by Bhagat *et al.*[33] They proved experimentally that circular hydraulic jumps during impingement of a normal jet on an infinite plane are independent of the orientation of the surface, i.e., it was discovered that gravity does not play a role in the origin/formation of the jumps contrary to previous theoretical analysis. The debate regarding the role of surface tension in hydraulic jumps is unresolved. Duchesne *et al.*[34] showed that the energy equation used by Bhagat *et al.* was flawed and provided a revised version of the equation. Previously, Duchesne and co-workers worked on the implications of constant Froude number on hydraulic jumps.[35] Later Bhagat *et al.* also studied the origin of the jump theoretically and showed that interfacial surface energy is not conserved due to a curved interface.[36] However, scientific literature that includes the evaporative effects on liquid film thickness and Nusselt numbers in the case of a laminar free jet impinging on a rotating heated plate is relatively sparse.

We study liquid film thickness and Nusselt numbers for a laminar axisymmetric free jet, impinging a rotating heated plate, including the evaporative effects. The analysis for various hydrodynamic to thermal boundary layer thickness ratios (greater than, equal to, and less than unity) in the high Froude number limit or equivalently in near zero-gravity conditions is performed. Scaling analysis from first principles has been used to decipher various limiting scales. The dependence of film thickness, the hydrodynamic and thermal boundary layers, the Nusselt number on the geometric parameters, and various non-dimensional parameters such as Prandtl, Reynolds, and the Rossby numbers is unearthed. First, the complexity of the physics results from the evaporative effects existing at the liquid–vapor interface compared with standard hydrodynamical interactions within a single liquid phase that are taken care of by terms in the Navier–Stokes equation. Second, coupling of the evaporative effects with the associated thermal energy equation exists, making the physics significantly more intricate. We tackle the first complexity and incorporate evaporative effects using an integral mass conservation equation coupled with the standard differential form of mass and linear momentum equations.[37–39] The complexity of coupling the evaporative effects and the thermal energy equation is solved by incorporating the energy equation's thermal boundary layer analysis[40] and the integral energy balance equation. Scalings of the fundamental equations were analyzed assuming constant evaporative flux. However, the results derived are general enough and can be extended to incorporate more complicated evaporative flux fields, which are not part of this study.

II. MATHEMATICAL MODELLING

A. Geometry and coordinate system

Figure 1 shows the schematic representation of a steady laminar jet impinging on a rotating heated plate. We have used a cylindrical axisymmetric coordinate system about the vertical z axis to formulate the conservation equations (mass, linear momentum, and thermal energy). CS denotes the control surface (shown in dotted red) bounding the control volume CV. The growing hydrodynamic boundary layer is denoted by BL, shown by the blue dotted line. The jet cross-section lies parallel to the r and z plane with the plate at $z = 0$. The jet impinges along the negative z direction (axial direction). The radial coordinate r has a length scale r_0, and the

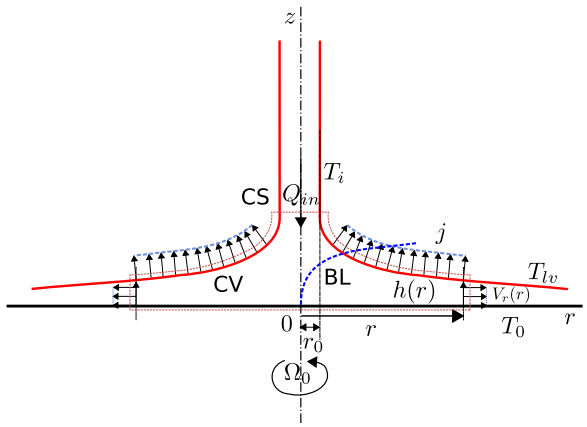

FIG. 1. Schematic representation of the axisymmetric laminar jet. Q_{in}, $h(r)$, and $\delta(r)$ represent the volume inflow rate, liquid film thickness, and boundary layer thickness, respectively. r_v denotes the radial location that the growing boundary layer meets the film thickness due to the jet. The plate is heated after $|r| > r_0$, and ω_0 denotes the rotational velocity of the disk. $V_r(r)$ denotes the average radial velocity of the liquid jet averaged over the liquid film thickness $h(r)$. T_i represents the temperature of the jet entering the control volume. T_0 is the bottom plate surface temperature, and T_{lv} is the liquid–vapor surface temperature. The evaporative flux is denoted by j.

axial coordinate has a length scale h_0. A circular rotating plate of an enormous radius R compared with r_0 lies in the horizontal plane ($R \gg r_0$). The plate rotates at a constant angular velocity of Ω_0. The inflow volume flow rate of the laminar jet is Q_{in}. The liquid film thickness profile is denoted by $h(r)$. $\delta(r)$ is the hydrodynamic boundary layer thickness, which grows with the radial coordinate r. The radial distance from the origin where $\delta(r)$ reaches a maximum is defined as r_v. The bottom plate is heated from $|r| \geq r_0$.

Conservation of mass, momentum, and energy in the cylindrical coordinate system has been used to develop various limiting scaling laws. The evaporation from the liquid film is incorporated in the analysis through a non-dimensional evaporation flux parameter.

B. Integral mass conservation

The jet, upon impinging the circular plate, rotating at an angular velocity of Ω_0 has an initial transient period. On reaching a steady state, the liquid film thickness profile $h(r)$ does not change anymore with time. Applying integral mass conservation inside the control volume (refer to Fig. 1) at a steady state, we have[37–40]

$$Q_{in} = V_r(r)2\pi rh(r) + \frac{1}{\rho}\int_{r_0}^{r} 2\pi r\sqrt{1+\left(\frac{\partial h}{\partial r}\right)^2}\,\mathbf{J}\cdot\mathbf{n}dr, \tag{1}$$

where $V_r(r)$ denotes the radial velocity averaged over the liquid film thickness. The first term on the left-hand side of Eq. (1) is the volume flow rate of the impacting jet entering the control volume. The second term on the right-hand side represents the volume of liquid flowing out of the control volume radially, and the third term on the right-hand side represents the mass loss from the control volume due to evaporative effects from the liquid film and air interface. Approximating the above equation by a scaling equivalent form by neglecting second order curvature effects and using $\mathbf{J}\cdot\mathbf{n} \sim const$, $\mathbf{J}\cdot\mathbf{n} \sim j = |D\nabla c|$, where c is the concentration field at the water air interface. Equation (1) reduces to

$$Q_{in} \sim V_r(r)2\pi rh(r) + \frac{j\pi}{\rho}(r^2 - r_0^2). \tag{2}$$

Rearranging and making average radial velocity the subject, $V_r(r)$ scales as

$$V_r(r) \sim \frac{1}{2\pi rh(r)}\left[Q_{in} - \frac{j\pi}{\rho}(r^2 - r_0^2)\right]. \tag{3}$$

C. Differential form of the continuity equation

The differential form of the continuity equation in an axisymmetric cylindrical coordinate system is[38,39]

$$\frac{1}{r}\frac{\partial(rV_r)}{\partial r} + \frac{\partial V_z}{\partial z} = 0. \tag{4}$$

The radial coordinate r scales as r_0 and, hence, Eq. (4) scales as

$$\frac{V_r}{r_0} \sim \frac{V_z}{z}. \tag{5}$$

Using the stream function formulation in cylindrical coordinates $\psi(r,z)$ for the radial and axial velocity field, we assured that the conservation of mass is valid at every point inside the control volume,

$$V_r = -\frac{1}{r}\frac{\partial\psi}{\partial z} \tag{6}$$

and

$$V_z = \frac{1}{r}\frac{\partial\psi}{\partial r}, \tag{7}$$

where V_r and V_z denote the radial and axial velocity components of the liquid film, respectively.

D. Differential stream function formulation of radial momentum equation

The stream function formulation[38,39] for the radial component of the Navier–Stokes equation under the thin film limit is given by

$$\frac{1}{r}\frac{\partial}{\partial r}\left[\frac{1}{r}\left(\frac{\partial\psi}{\partial z}\right)^2\right] - \frac{\partial}{\partial z}\left[\frac{1}{r^2}\frac{\partial\psi}{\partial z}\frac{\partial\psi}{\partial r}\right] = \Omega_0^2 r - \nu\frac{\partial^2}{\partial z^2}\left[\frac{1}{r}\frac{\partial\psi}{\partial z}\right]. \tag{8}$$

The circumferential velocity scale of fluid is approximately equal to tangential linear velocity due to rotation at the bottom of the plate due to no-slip boundary condition. The 2D approximation holds for relatively low to moderate angular speeds, low jet velocity and thus, at higher Rossby number and relatively small Reynolds number. At very higher rotation rates, the hydrodynamics becomes completely 3D and 2D analysis cannot be used.[3,25,41] The assumptions of the circumferential velocity have been used in the previous literature[20] to estimate heat transfer characteristics from a semi-analytical framework. Introducing the scales of various terms in Eq. (8). The average radial velocity scales as $V_r \sim V_*$, the stream function scales as $\psi \sim rV_*z$, and the axial velocity scales as $V_z \sim \frac{1}{r}V_*z$. Therefore, Eq. (8) can be rewritten in a scaling form as

$$\frac{V_*^2}{r} \sim \Omega_0^2 r, \quad \frac{\nu V_*}{z^2}. \tag{9}$$

Note that Eq. (9) does not depict a dominant balance of the various physical scales represented by the terms of the equation. It represents the scales of the various terms (the left-hand side [LHS] and right-hand side [RHS]) of Eq. (8). The comma in Eq. (8) is used as a delimiter to indicate the distinct scales in the R.H.S. of Eq. (8). We can observe three dominant physical scales that can exist. The scale in the LHS of Eq. (9) represents the advection of radial momentum (inertial term); the first term on the RHS represents the radial momentum transfer due to rotation while the second term on the RHS represents momentum diffusion.

E. Differential form of the energy equation

The differential form of the thermal energy equation[40] for the temperature field $T(r,z)$ is

$$\frac{1}{r}\frac{\partial}{\partial r}(rV_rT) + \frac{\partial}{\partial z}(V_zT) = \alpha\left(\frac{\partial^2 T}{\partial z^2} + \frac{1}{r}\frac{\partial}{\partial r}\left(r\frac{\partial T}{\partial r}\right)\right). \tag{10}$$

Using the scales $r \sim r_0$, $z \sim \delta_T$, the scaling form of Eq. (10) in the thermal boundary layer limit becomes

$$\frac{V_r \Delta T}{r_0}, \quad \frac{V_z \Delta T}{\delta_T} \sim \frac{\alpha \Delta T}{\delta_T^2}. \tag{11}$$

Equation (11) represents all the dominant scales of the thermal energy equation inside the thermal boundary layer. Note that the comma is used a delimiter to separate the various scales possible in a given equation. The first and second terms on the left-hand side of Eq. (11) represent the radial and axial convective terms, respectively. The third term on the right-hand side represents the axial thermal diffusive term. The fundamental relations in this section such as Eqs. (3), (5), (9), and (11) have been used to derive the scalings for liquid film thickness and Nusselt number as presented in the results and discussion section.

III. RESULTS AND DISCUSSIONS

The analysis required to calculate the scales of liquid film thickness and Nusselt number depends on various limiting conditions discussed below in separate subsections. The scale of liquid film thickness height profile $h(r)$ and Nusselt number $Nu(r)$ is an intricate function that depends on the interaction between the inertial, rotation, viscous, and evaporative effects. We will start by evaluating the liquid film thickness scale under various limiting conditions/cases. Subsections III A 1 and III A 2 deals with certain mathematical limiting cases, and we present these sections to introduce the scaling methodology, that is, being used throughout the article. Subsection III A 1 deals with a special inviscid case and is a direct corollary of Eq. (9). This case deals with the balance between the first term on the LHS and the first term on the RHS of Eq. (9). Note that Subsection III A 1 is a very special mathematical case and does not imply a general condition. Subsection III A 2 deals with another special inviscid case with zero rotation. Section III A 3 describes a third limiting case that can exist as a balance between the rotation and viscous scales of Eq. (9). The viscous rotation scale developed in Sec. III A 3 deals with flows having large angular velocities or thicker jets at relatively small flow rates.

A. Liquid film thickness

1. Inertial inviscid rotation scaling with the variable scale for radial velocity

The radial velocity scale V_* averaged over the film thickness from Eq. (3) equated with the variable rotational velocity scale $(\Omega_0 r)$ results in a scaling relation for the liquid film thickness. This scaling physically signifies a rigid body type of motion for the entire liquid film.[37–39] Note that this comparison is only made for the velocity scale, which has a linear dependence on radial coordinate, which is similar to a rigid body velocity distribution. It has no physical implications on the actual flow state, which itself is a special case,

$$V_* \sim \Omega_0 r \sim \frac{1}{2\pi r h(r)}\left[Q_{in} - \frac{j\pi}{\rho}\left(r^2 - r_0^2\right)\right]. \tag{12}$$

The liquid film thickness scale becomes

$$h(r) \sim \frac{1}{2\pi \Omega_0 r^2}\left[Q_{in} - \frac{j\pi}{\rho}\left(r^2 - r_0^2\right)\right]. \tag{13}$$

Substituting $Q_{in} = 2\pi r_0 h_0 V_0$ (refer to Fig. 1), we have

$$h(r) \sim \frac{Q_{in}}{2\pi \Omega_0 r^2}\left[1 - \frac{j\pi}{\rho Q_{in}}\left(r^2 - r_0^2\right)\right]. \tag{14}$$

Let $E(r)$ denote the evaporation factor given by

$$E(r) = \left[1 - \frac{j\pi r_0^2}{\rho Q_{in}}\left(\frac{r^2}{r_0^2} - 1\right)\right]. \tag{15}$$

Introducing a nondimensional group to form a change of variables, we have

$$\beta = \frac{j\pi r_0^2}{\rho Q_{in}}, \tag{16}$$

$$E(r) = \left[1 - \beta\left(\frac{r^2}{r_0^2} - 1\right)\right]. \tag{17}$$

Equation (15) is plotted in Fig. 2. The non-dimensional factor β is the ratio of the evaporative mass loss through an area of πr_0^2 to the mass flow rate inside the control volume CV. $\beta = 0$ represents zero evaporative flux through the liquid–air interface that is physically equivalent to a saturated environment (hundred percent relative humidity). The second term in the definition of $E(r)$ is $\beta(r^2/r_0^2 - 1)$, which represents the ratio of the evaporative mass loss through the liquid–vapor interface to the mass flow rate inside the control volume CV. The effect of β and the radial coordinate on the evaporation factor $E(r)$ can be inferred from Fig. 2. $E(r)$ decreases as the radial coordinate and the non-dimensional factor β increases. Using the above change of variables and representing the liquid film thickness as a fraction of a vertical length scale h_0 [mostly the vertical entrance scale in experiments reported in literature[4] Eq. (14)] can be rewritten as

$$\frac{h(r)}{h_0} \sim \left(\frac{r_0}{r}\right)^2 \sqrt{Ro} E(r), \tag{18}$$

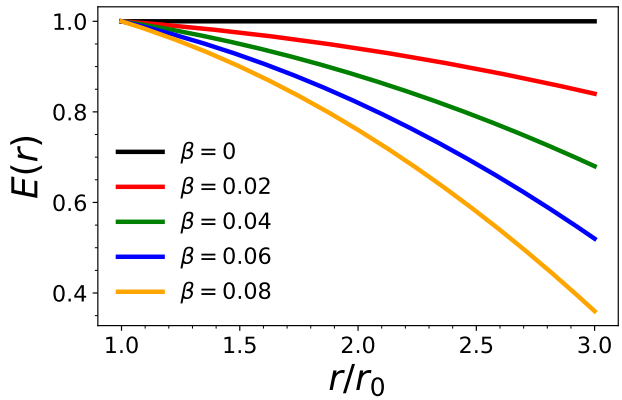

FIG. 2. Evaporation factor $E(r)$ plotted as a function of normalized radial distance r/r_0 with β as a parameter. Five different values of $\beta \sim j\pi r_0^2/\rho Q_{in}$ are shown, representing different amounts of evaporation from the free liquid surface of the jet.

$$Ro = \frac{V_0^2}{\Omega_0^2 r_0^2}, \tag{19}$$

where Ro is the Rossby number. We use a non-standard naming convention for the Rossby number. The logic behind using the Rossby number to characterize the centrifugal term is due to the mathematical form of the term that appears in the radial momentum equation. Refer to Basu and Cetegen for the details.[20] Since dominant physical parameter is rotation, the velocities are normalized with the linear velocity associated with the angular velocity at a radial distance r_O. Note that this term appears in the radial momentum equation and is physically related to the centrifugal force rather than the Coriolis force, which acts in the tangential direction. Equation (18) signifies the physical scaling of liquid film thickness under the effect of a rigid body rotation of the liquid film and inertia. Figure 3(a) compares the liquid film thickness for different Rossby numbers and zero evaporative flux. The film thickness scaling was plotted using Eq. (18). On increasing the Rossby number (i.e., decreasing rotational angular velocity Ω_0), the liquid film thickness increases. The effect of evaporation on the liquid film thickness can be understood from Fig. 3(b). Figure 3(b) represents the liquid film thickness for a fixed Rossby number $Ro \sim 1$ and a variable evaporative flux. The effect of evaporative flux becomes important as the radial coordinate increases. Note that the numerical value of $\beta = 0.08$ used is the maximum upper limit possible and it corresponds to the maximum evaporation flux that the flow can sustain before forming hot spots along the plate where the film thickness asymptotically tends to zero.

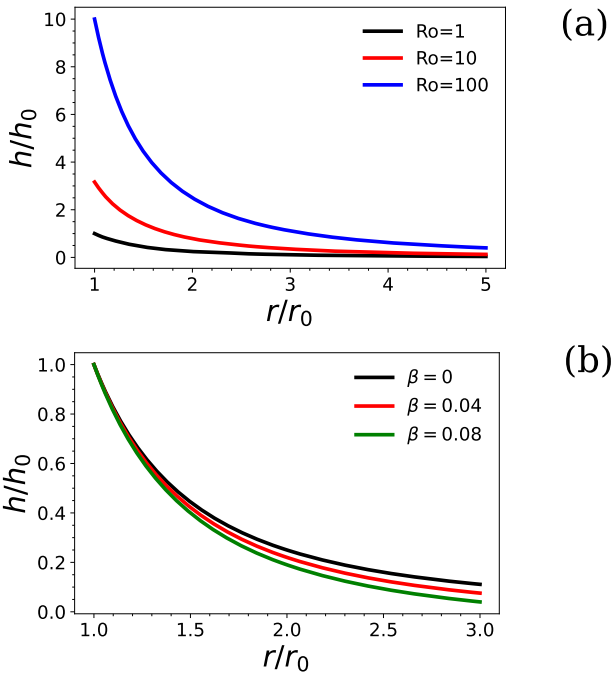

FIG. 3. The liquid film thickness profile plotted as a function of the radial coordinate for the inertia-rotation limit. (a) Dependence of the liquid profile with the Rossby number as a parameter. (b) Dependence of the liquid profile with β used as a parameter.

2. Inertial inviscid scaling with a constant scale for radial velocity ($\Omega_0 = 0$)

A different scaling limit exists for liquid film thickness by using a constant radial velocity scale ($V_* \sim V_0$), which physically resembles the situation of zero rotation of the plate. Using Eq. (3) to assure integral mass conservation, the radial velocity scales as

$$V_* \sim V_0 \sim \frac{1}{2\pi r h(r)}\left[Q_{in} - \frac{j\pi}{\rho}(r^2 - r_0^2)\right]. \tag{20}$$

Simplifying further and using $Q_{in} = 2\pi r_0 h_0 V_0$, we have

$$\frac{h(r)}{h_0} \sim \frac{r_0}{r}\left[1 - \frac{j\pi r_0^2}{\rho Q_{in}}\left(\frac{r^2}{r_0^2} - 1\right)\right]. \tag{21}$$

Rewriting Eq. (21) using the evaporation factor $E(r)$ from Eq. (17), we have

$$\frac{h(r)}{h_0} \sim \frac{r_0}{r}E(r). \tag{22}$$

Comparing Eqs. (18) and (22), we observe that the dependence on the evaporation factor is the same (linear on $E(r)$). Increased evaporation flux corresponds to larger β and smaller $E(r)$ and, hence, smaller liquid film thickness. However, the liquid film thickness falls off faster $(1/r^2)$ in the case of rotation scaling compared with zero rotation $(1/r)$.

3. Viscous rotation scaling

In practical applications involving liquid jet impingement on high speed rotating plates, viscous effects in addition to rotational effects are important due to high gradients of the velocity in a very thin region near the plate. In this section, the effects of rotation are now included to counteract the viscous effects. Equating the viscous and rotation scaling from Eq. (9), we have

$$\frac{\nu V_*}{z^2} \sim \Omega_0^2 r. \tag{23}$$

The inertial term in Eq. (9) scales as V_*^2/r (inversely proportional to radius) and, therefore, dominates for small values of r ($r \sim r_0$). For small values of r, i.e., near the entry point of the impinging jet, $V_* \sim V_0$. The rotation term on the other hand increases linearly with radial coordinate r. The viscous term increases with the radial coordinate as the film thickness decreases with an increase in the radial coordinate and, hence, cannot be neglected. Comparing the scales for the inertial and rotation term near the inlet gives $V_0 \sim \Omega_0 r_0$. The critical radius, therefore, becomes $r_c \sim V_0/\Omega_0$. Therefore, the condition for the applicability of viscous-rotation scaling is $r_c < r_0$, which simplifies to $V_0 < \Omega_0 r_0$. The balance described can be achieved physically at a comparable radius to r_0 for sufficiently large angular velocities or thicker jets with small flow rates. For evaluating the scale of liquid film thickness $h(r)$, we can scale $z \sim h(r)$,

$$\frac{\nu V_*}{h^2} \sim \Omega_0^2 r. \tag{24}$$

Using Eq. (3) in Eq. (24), we can establish a scale for the liquid film thickness incorporating the effects of viscosity, rotation, and evaporation. Therefore, the scales of Eq. (24) can be rewritten as

$$V_* \sim \frac{\Omega_0^2 r h^2(r)}{\nu} \sim \frac{1}{2\pi r h(r)}\left[Q_{in} - \frac{j}{\rho}(r^2 - r_0^2)\right]. \tag{25}$$

Simplifying and non-dimensionalizing $h(r)$, we have

$$\frac{h(r)}{h_0} \sim \left(\frac{Ro}{Re}\right)^{1/3}\left(\frac{r_0}{h_0}\right)^{2/3}\left(\frac{r_0}{r}\right)^{2/3}\left[1 - \frac{j\pi r_0^2}{\rho Q_{in}}\left(\frac{r^2}{r_0^2} - 1\right)\right]^{1/3}, \tag{26}$$

where Ro is the Rossby number and

$$Re = \frac{V_0 r_0}{\nu}. \tag{27}$$

Using the definition of $E(r)$, Eq. (26) can be rewritten as

$$\frac{h(r)}{h_0} \sim \left(\frac{Ro}{Re}\right)^{1/3}\left(\frac{r_0}{h_0}\right)^{2/3}\left(\frac{r_0}{r}\right)^{2/3}[E(r)]^{1/3}. \tag{28}$$

Equation (28) shows the dependence of the normalized liquid film thickness on the Rossby number, Reynolds number, and the evaporation factor, respectively (Ro, Re, and $E(r)$). The liquid film thickness for viscous-rotation limit scales as $1/r^{2/3}$, which is different from the previous scalings derived before [refer to Eqs. (18) and (22)]. Figures 4(a) and 4(b) show the dependence of the liquid film thickness profile on the Reynolds number and Rossby number. Increasing the Rossby number (decreasing angular velocity Ω_0) increases the liquid film thickness ($h(r)/h_0 \sim Ro^{1/3}$) provided all the parameters are unchanged. The liquid film thickness is inversely proportional to the Reynolds number ($h(r)/h_0 \sim Re^{-1/3}$) as shown in Fig. 4(b). The dependence on the evaporation factor is non-linear ($h(r)/h_0 \sim [E(r)]^{1/3}$). This scaling law is different from Eqs. (18) and (22) where the dependence on the evaporation factor is linear. Note that the evaporation factor is always less than one (refer to Fig. 2, $E(r) < 1$). Equation (28) has the same form as the closed-form solutions derived by Basu and Cetegen for negligible inertia.[19] The height profile given by Eq. (28) (viscous-rotation scale) conforms with the scale derived by (Wang and Khayat 2018)[31] [refer to Eq. (4.13) of Wang *et al.* 2018 and Eq. (28) here]. The dependence on various parameters such as Reynolds number, angular speed, and radial coordinate is exactly the same. Note that the correlations were derived from pure scaling logic, without any velocity profile assumption previously used in the literature. Figure 5 compares the liquid film thickness scaling against some previous numerical and experimental data from the literature.[4,11] The graph shows the variation of liquid film thickness profile at a fixed Reynolds number with angular velocity (Rossby Number) as a parameter. The numerical coefficients used to compare the scaling results with experimental values were evaluated using the geometric form factor of the system. For a particular experimental condition corresponding to specific values of Reynolds (Re) and Rossby number (Ro), we equate the experimental film thickness to the thickness predicted from the scalings law at a fixed radial coordinate r. The numerical coefficient used for the comparison is the ratio of experimental film thickness to the theoretical scaling obtained at a fixed radial coordinate. We use a similar methodology to compare the experimental and theoretical scales for the Nusselt number presented later in the text. Increasing the angular velocity decreases the liquid film thickness. The scalings predicted [refer to Fig. 4(b)] were in agreement with the experimental data reported in the literature.

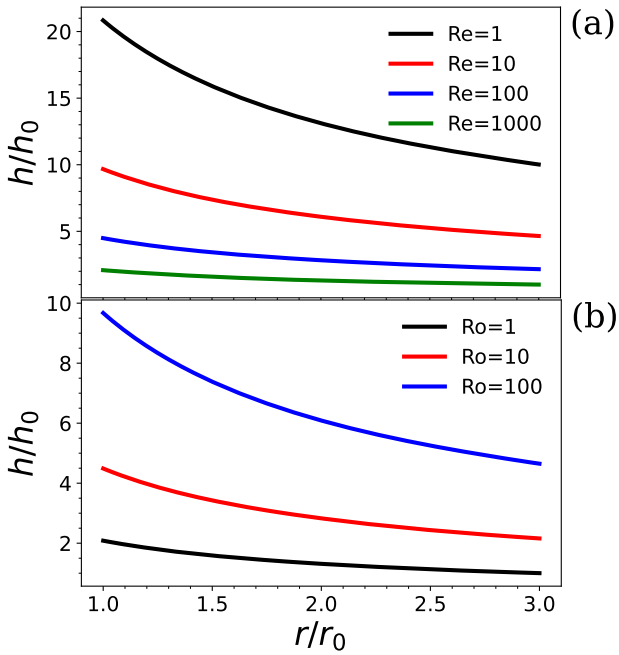

FIG. 4. The liquid film thickness profile plotted as a function of the radial coordinate for the viscous-rotation limit. (a) Dependence of the liquid profile with the Reynolds number as a parameter. (b) Dependence of the liquid profile with the Rossby number as a parameter.

B. The average radial velocity field scaling

In this section, we derive the average radial velocity scales for the viscous rotation limit. From Eq. (25), the average radial velocity scales as

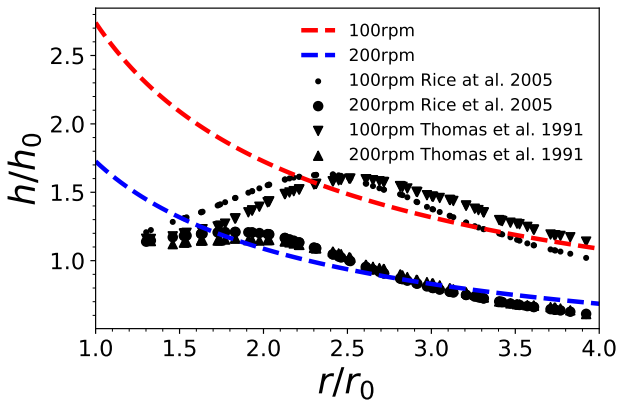

FIG. 5. The viscous-rotation scaling limit of liquid film thickness compared with experimental and numerical data from the literature. The dashed line depicts the scales predicted using scaling theory.

$$V_* \sim \frac{\Omega_0^2 r h^2(r)}{\nu}. \tag{29}$$

Defining $V_\dagger = \Omega_0 r_0$ and using Eq. (24) in Eq. (28), we have

$$\frac{V_*}{V_\dagger} \sim Ro^{2/3} Re^{1/3} \left(\frac{r_0}{h_0}\right)^{4/3} \left(\frac{r_0}{r}\right)^{1/3} E(r)^{2/3}. \tag{30}$$

Equation (30) deciphers the scales of the radial velocity on Ro, Re, r, and $E(r)$. The dependence on the radial coordinate is $\sim r^{-1/3}$. This shows the radial velocity decreases with radius. The physical condition is equivalent to the velocity field inside hydrodynamic boundary layers.

C. Hydrodynamic boundary layer thickness

The heat transfer characteristics such as the Nusselt number and the average temperature distribution of the liquid film can be understood in terms of boundary layer analysis. This section looks into the hydrodynamic boundary layer scalings, which will further lead to thermal boundary layer analysis in the later sections. The radial flow velocity in the liquid rises very sharply from zero to the free surface jet velocity in a very thin boundary layer region. Viscous forces balance inertial effects inside the boundary layer. From the viscous scaling inside the boundary layer [using Eq. (9) and $z \sim \delta$], the boundary layer thickness scale for $r < r_v$ (r_v defined below) is

$$\frac{V_*^2}{r} \sim \frac{\nu V_*}{\delta^2}. \tag{31}$$

The analysis is carried out in a rotating frame attached to the rotating hot plate. Hence, the role of rotation can be thought of as a centrifugal body force term that effects the radial velocity scale V^*. However, the centrifugal force is not constant changes with radial coordinate becoming stronger as the radius increases. The effect of the centrifugal term was incorporated inside the boundary layer through V_* that was evaluated through the viscous rotation scaling of V_* in Eq. (30). Using the scale of (V_*) from Eq. (30) in Eq. (31), the boundary layer thickness scales as

$$\frac{\delta}{r_0} \sim Re^{-2/3} Ro^{-1/12} \left(\frac{r_0}{h_0}\right)^{-2/3} \left(\frac{r}{r_0}\right)^{2/3} [E(r)]^{-1/3}. \tag{32}$$

The radial location at which the boundary layer profile peak is represented by r_v [see Fig. 6(a)]. Equation (32) shows the dependence of the boundary layer thickness on the radial coordinate, Rossby number, Reynolds number, and evaporation factor for $r < r_v$ For $r > r_v$, the boundary layer thickness scales as the liquid film thickness for the viscous rotation scaling given by

$$\frac{\delta}{r_0} \sim \frac{h(r)}{r_0} \sim \left(\frac{Ro}{Re}\right)^{1/3} \left(\frac{h_0}{r_0}\right)^{1/3} \left(\frac{r_0}{r}\right)^{2/3} E(r)^{1/3}. \tag{33}$$

Equations (32) and (33) define the boundary layer thickness scales in a piecewise manner. This piecewise function δ is plotted as a function of the radial coordinate for $Ro \sim \mathrm{Re} \sim 1$ and $\beta = 0$ in Fig. 6(b). Comparing Eq. (32) with (33) depicts that the effects of

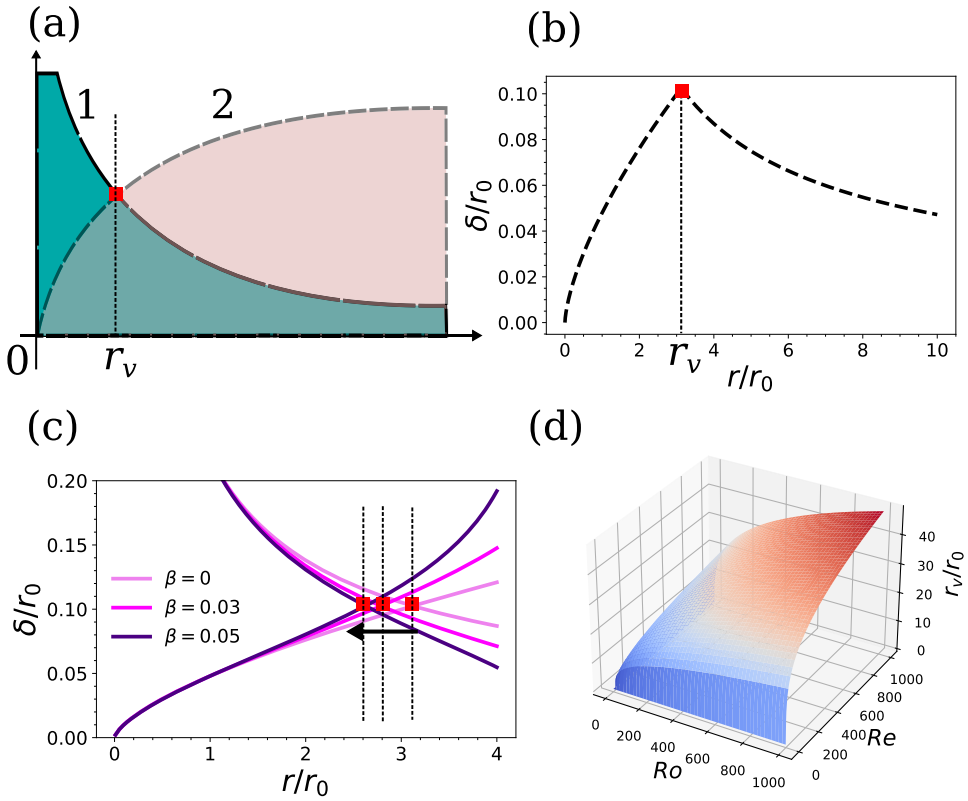

FIG. 6. (a) Schematic representation (not to scale) of the liquid film profile (shown by 1) and boundary layer profile (shown by 2). The intersection of profiles 1 and 2 defines the radial location r_v where the boundary layer profile reaches a maximum. (b) The combined piecewise boundary layer profile plotted for $Ro \sim \mathrm{Re} \sim 1$ and $\beta = 0$. (c) The effect of β on the combined boundary layer profile. (d) A surface plot showing the dependence of r_v/r_0 on the Rossby number and Reynolds number for $\beta = 0$.

Rossby number and evaporation factor on liquid film thickness are reversed before and after the critical radius r_v.

D. Scaling of the radial location r_v

The radial location r_v is the distance where the viscous boundary layer from the plate meets the outer liquid film thickness profile in the viscous rotation scaling [refer to Figs. 6(a) and 6(b)]. The existence of r_v is only valid for cases where the thermal boundary is much smaller than 1, i.e., $\delta/\delta_T \gg 1$. Equating the scales of Eqs. (32) and (33) and solving for r_v in case of $E(r) = 1$ (i.e., no evaporation), we have

$$\frac{r_v}{r_0} \sim \left(\frac{r_0}{h_0}\right)^{1/4} Ro^{5/16} Re^{1/4}. \tag{34}$$

The effect of evaporation on the radial coordinate r_v can be inferred from Fig. 6(c). Increased evaporation flux rate reduces r_v. It can be observed by the shift in the intersection position [shown as a red solid square in Fig. 6(c)] of the initial increasing boundary layer profile and the decreasing liquid film thickness profile. Equation (35) shows the dependence of r_v on Ro and Re for $\beta = 0$. The dependence is visualized as a surface map shown in Fig. 6(d).

For $0 < E(r) < 1$, the scale of r_v/r_0 can be solved explicitly by keeping the terms of $E(r)$ after equating the scales of Eqs. (32) and (33),

$$Re^{-2/3} Ro^{-1/12} \left(\frac{r_0}{h_0}\right)^{-2/3} \left(\frac{r_v}{r_0}\right)^{2/3} [E(r_v)]^{-1/3} \sim Ro^{1/3} Re^{-1/3} \left(\frac{r_0}{h_0}\right)^{-1/3} \left(\frac{r_v}{r_0}\right)^{-2/3} [E(r_v)]^{1/3}. \tag{35}$$

Equation (35) can be simplified and solved explicitly for r_v/r_0 in this case (note algebraically that this is not always possible),

$$\frac{r_v}{r_0} \sim \sqrt{\frac{1+\beta}{\beta + F(Ro, Re, r_0, h_0)}}, \tag{36}$$

where

$$F(Ro, Re, r_0, h_0) = Ro^{-5/8} Re^{-1/2} \left(\frac{r_0}{h_0}\right)^{-1/2}. \tag{37}$$

Equation (36) is plotted in Figs. 7(a) and 7(b). Figure 7(a) depicts the dependence of the critical radius r_v on β with the Rossby number as the parameter. Similarly, Fig. 7(b) depicts the dependence of the critical radius r_v on β with the Reynolds number as the parameter. Both Figs. 7(a) and 7(b) show that the critical length scale r_v decreases with increasing β, i.e., increased evaporation rate.

E. Thermal boundary layer thickness and Nusselt number for $\delta/\delta_T \sim 1$

In this and the following two sections, we discuss the thermal characteristics for various limiting cases. We calculate the Nusselt number scaling for $\delta/\delta_T \sim 1$, $\delta/\delta_T > 1$, and $\delta/\delta_T < 1$. As discussed in Sec. III C, the hydrodynamic boundary layer thickness scalings can be defined in a piecewise manner using two limiting conditions. Following a similar line of reasoning for the thermal boundary layer and Nusselt number, we have two regimes $r < r_v$ and $r > r_v$. For $r < r_v$, the thermal boundary layer height scales as the hydrodynamic

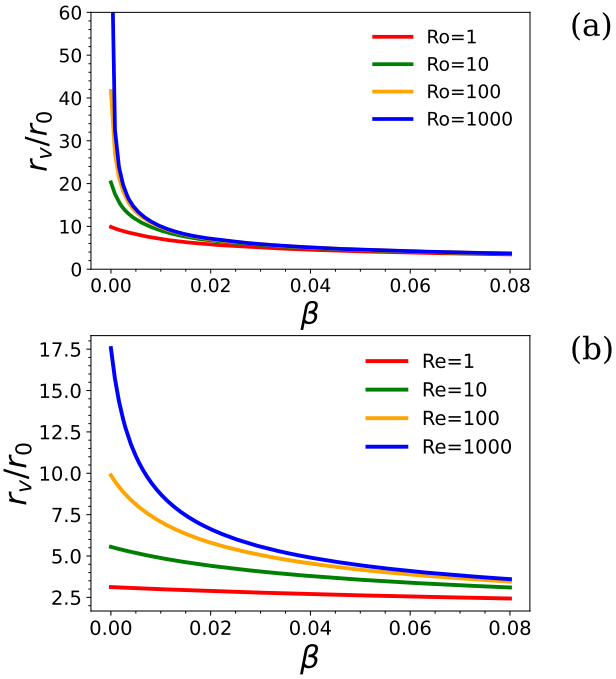

FIG. 7. (a) The variation of r_v/r_0 with respect to β with the Rossby number as the parameter for $Re \sim 1$. (b) The variation of r_v/r_0 with respect to β with the Reynolds number as the parameter for $Ro \sim 1$.

boundary layer ($\delta \sim \delta_T$). The thermal boundary layer thickness from Eq. (32) can be written, therefore, as

$$\frac{\delta_T}{r_0} \sim \frac{\delta}{r_0} \sim Re^{-2/3} Ro^{-1/12} \left(\frac{r_0}{h_0}\right)^{-2/3} \left(\frac{r}{r_0}\right)^{2/3} [E(r)]^{-1/3}. \tag{38}$$

Simplifying further, the thermal boundary layer thickness written in terms of non-dimensional parameters such as Rossby number (Ro) and Reynolds number (Re) is

$$\frac{\delta_T}{r_0} \sim Re^{-1/2} Ro^{1/4} \left(\frac{r}{r_0}\right)^{1/2} \left(\frac{V_*}{V_\dagger}\right)^{-1/2}. \tag{39}$$

Using Eq. (30) in Eq. (39) for $V_*/V_\dagger$,

$$\frac{\delta_T}{r_0} \sim Re^{-2/3} Ro^{-1/12} \left(\frac{r_0}{h_0}\right)^{-2/3} \left(\frac{r}{r_0}\right)^{2/3} [E(r)]^{-1/3}. \tag{40}$$

The Nusselt number scale is the reciprocal of the nondimensional thermal boundary layer thickness scale,

$$Nu \sim \frac{r_0}{\delta_T} \sim Re^{2/3} Ro^{1/12} \left(\frac{r_0}{h_0}\right)^{2/3} \left(\frac{r}{r_0}\right)^{-2/3} [E(r)]^{1/3}. \tag{41}$$

For $r > r_v$, the boundary layer length scales as the liquid film thickness [refer to Eq. (33)],

$$\frac{\delta}{r_0} = \frac{\delta_T}{r_0} \sim \left(\frac{h_0}{r_0}\right)^{1/3} \left(\frac{Ro}{Re}\right)^{1/3} \left(\frac{r_0}{r}\right)^{2/3} [E(r)]^{1/3}. \tag{42}$$

The Nusselt number scaling can be rewritten as

$$Nu \sim \frac{r_0}{\delta_T} \sim \left(\frac{h_0}{r_0}\right)^{-1/3}\left(\frac{Ro}{Re}\right)^{-1/3}\left(\frac{r_0}{r}\right)^{-2/3}[E(r)]^{-1/3}. \quad (43)$$

Figure 8(a) shows the variation of the Nusselt number limiting scales with a radial coordinate for $Ro \sim 1$, $Re \sim 1$, $Pr \sim 7$, and β as the parameter. For $0 < r/r_0 < r_v/r_0$, the Nusselt number decreases with the radial coordinate due to an increasing thermal boundary layer thickness scale. The Nusselt number scales increase with radial coordinate $r/r_0 > r_v/r_0$ due to subsequent reduction of liquid film thickness. Equations (41) and (43) together show the dependence on the Rossby number, Reynolds number, and the evaporation factor in a piecewise manner for $r < r_v$ and $r > r_v$, respectively. The dependence of the Nusselt number Nu on evaporation factor $E(r)$ is reversed before and after the critical length scale r_v. It can be inferred from Fig. 8(a) that the increased evaporation flux (higher value of β) causes an increase in the Nusselt number.

F. Thermal boundary layer thickness and Nusselt number for $\delta/\delta_T \gg 1$

This section develops the thermal characteristics scales for conditions where the hydrodynamic boundary layer thickness is very much greater than the thermal boundary layer thickness. From Eq. (22), we have the scaling form of the thermal energy equation inside the thin thermal boundary layer region,

$$\frac{V_r \Delta T}{r_0}, \frac{V_z \Delta T}{\delta_T} \sim \frac{\alpha \Delta T}{\delta_T^2}. \quad (44)$$

Since the thermal boundary layer is wholly immersed inside the hydrodynamic boundary layer, there exists a gradient of radial velocity in the z-direction inside the thermal boundary layer. The radial velocity scale inside the thermal boundary layer is, therefore, given by

$$V_r \sim \frac{V_* \delta_T}{\delta}. \quad (45)$$

From the scaling form of Eq. (4), the relationship between the radial velocity V_r and the axial velocity V_z is

$$\frac{V_r}{r_0} \sim \frac{V_z}{\delta_T}. \quad (46)$$

Using Eq. (45) in Eq. (46), the axial velocity scales as

$$V_z \sim \frac{\delta_T V_r}{r_0} \sim \frac{V_* \delta_T^2}{r_0 \delta}. \quad (47)$$

Using the scales of V_r and V_z from Eqs. (45) and (47), respectively, in Eq. (44), the scaling form of the thermal energy equation becomes

$$\frac{V_* \delta_T}{r_0 \delta}, \frac{V_* \delta_T^2}{r_0 \delta \delta_T} \sim \frac{\alpha}{\delta_T^2}. \quad (48)$$

The first and second term scales in Eq. (48) are equivalent and, therefore, Eq. (48) can be rewritten as

$$\frac{V_*}{r_0}\frac{\delta_T}{\delta} \sim \frac{\alpha}{\delta_T^2}, \quad (49)$$

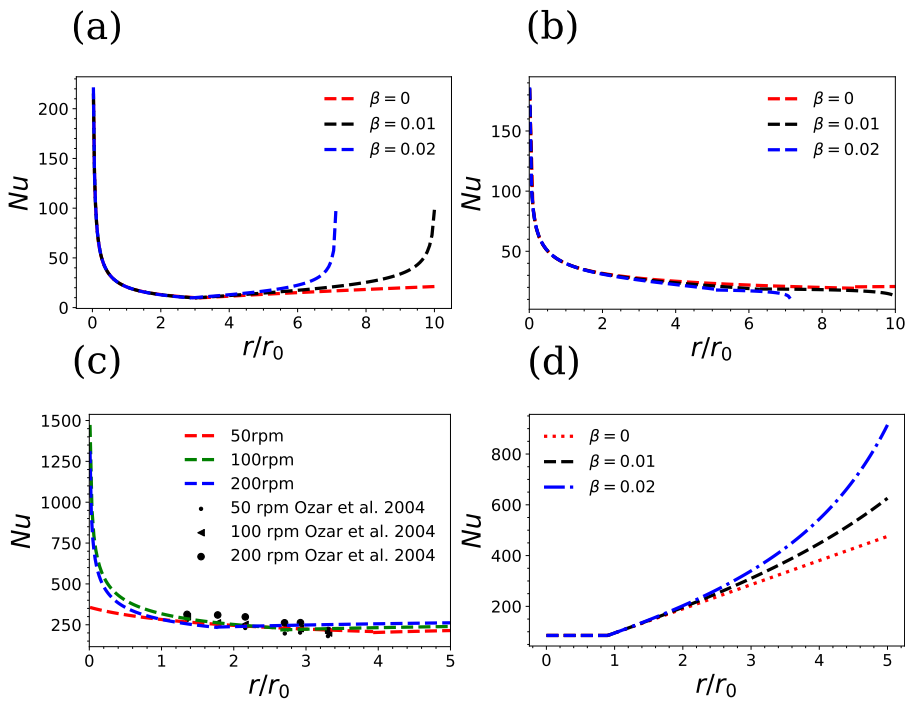

FIG. 8. (a) Nusselt number scales plotted as a function of the radial coordinate for $\delta \sim \delta_T$ for $Ro \sim Re \sim 1$, $Pr = 7$, and β as the parameter. (b) Nusselt number scales plotted as a function of the radial coordinate for $\delta \gg \delta_T$ for $Ro \sim Re \sim 1$, $Pr \sim 7$, and β as the parameter. (c) Nusselt number scales comparison with experimental and numerical data available from the literature. The dashed lines represent the scales predicted for the Nusselt number. (d) Nusselt number scales plotted as a function of the radial coordinate for $\delta \ll \delta_T$ for $Re \sim 10\,000$, $Pr = 0.1$, and β as the parameter.

$$\left(\frac{\delta_T}{r_0}\right)^3 \sim \frac{\alpha}{V_* r_0}\frac{\delta}{r_0}. \tag{50}$$

Equation (50) can be simplified using non-dimensional numbers and rewritten as

$$\left(\frac{\delta_T}{r_0}\right)^3 \sim Pe^{-1} Ro^{1/2}\left(\frac{V_\dagger}{V_*}\right)\left(\frac{\delta}{r_0}\right), \tag{51}$$

where $Pe = \mathrm{RePr} = V_0 r_0/\alpha$ is the Peclet number. The boundary layer thickness for $r < r_T$ (r_T is the radial coordinate at which the thermal boundary layer meets the liquid film thickness) is given by Eq. (32). Substituting the value of δ/r_0 in Eq. (51) and solving for δ_T/r_0,

$$\frac{\delta_T}{r_0} \sim Pr^{-1/3} Re^{-2/3} Ro^{-1/12}\left(\frac{r_0}{h_0}\right)^{-2/3}\left(\frac{r}{r_0}\right)^{1/3}[E(r)]^{-1/3}. \tag{52}$$

Hence, the scale for the Nusselt number can be calculated using the above equation,

$$Nu \sim \frac{r_0}{\delta_T} \sim Pr^{1/3} Re^{2/3} Ro^{1/12}\left(\frac{r_0}{h_0}\right)^{2/3}\left(\frac{r}{r_0}\right)^{-1/3}[E(r)]^{1/3}. \tag{53}$$

For $r > r_T$, substituting the scale of the hydrodynamic boundary layer thickness from Eq. (33) into Eq. (51) the thermal boundary layer scales as

$$\left(\frac{\delta_T}{r_0}\right) \sim Pr^{-1/3} Ro^{1/18} Re^{-5/9}\left(\frac{r_0}{h_0}\right)^{23/45}\left(\frac{r_0}{r}\right)^{1/9}[E(r)]^{-1/9}. \tag{54}$$

Hence, the Nusselt number scales as

$$Nu \sim Pr^{1/3} Ro^{-1/18} Re^{5/9}\left(\frac{r_0}{h_0}\right)^{-23/45}\left(\frac{r_0}{r}\right)^{-1/9}[E(r)]^{1/9}. \tag{55}$$

Equation (53) along with (55) defines Nusselt number scales in a piecewise manner. Figure 8(b) depicts the scales of the Nusselt number in a graphical way for water (having $Pr \sim 7$, $Ro \sim Re \sim 1$, and β as the parameter). The effect of evaporation (β) on the Nusselt number in this case is negligible as can be inferred from Fig. 8(b), which is different from the case when $\delta_T \sim \delta$ [refer to Fig. 8(a)]. The Nusselt number decreases with radial coordinate continuously. This can be attributed to the fact that the thermal boundary layer is very small compared with the liquid film thickness and just keeps growing reducing the Nusselt number. Figure 8(c) shows the Nusselt number comparison with some previous references available from the literature.[3] The scales predicted from analysis are consistent with the experimental data.

G. Scaling of r_T for $\delta/\delta_T \gg 1$

The radial coordinate r_T is the distance from the axis of rotation where the thermal boundary layer intersects the liquid film thickness profile. The scale for r_T can be deduced by equating the scales from Eqs. (52) and (33). However, unlike the case for $\delta_T \sim \delta$, the scale for r_T cannot evaluated algebraically. The equation relating the scales of r_T with other parameters is

$$\left(\frac{r_T}{r_0}\right)^{-3/2}[E(r_T)] \sim G(Ro, Re, Pr, r_0, h_0), \tag{56}$$

where

$$G(Ro, Re, Pr, r_0, h_0) = Ro^{-5/8} Re^{-1/2} Pr^{-1/2}\left(\frac{r_0}{h_0}\right)^{-1/2}. \tag{57}$$

We have solved Eq. (56) for r_T/r_0 graphically using three different values of $\beta = 0, 0.01, 0.02$. Figure 9(a) shows the graphical solution for r_T. It can be inferred from Fig. 9(a) that the critical length scale r_T decreases with an increase in evaporation flux represented by β. The vertical axis $H(r_T/r_0)$ in Fig. 9(a) is a function of r_T/r_0 with β as a parameter,

$$H(r_T/r_0) = \frac{1-\beta}{(r_T/r_0)^{3/2}} - \beta(r_T/r_0)^{1/2}. \tag{58}$$

From Fig. 9(a), the values of r_T/r_0 can be evaluated. r_T/r_0 calculated are 8.9 for $\beta = 0$, 6.3 for $\beta = 0.01$ and 5.1 for $\beta = 0.02$.

H. Thermal boundary layer thickness and Nusselt number for $\delta/\delta_T \ll 1$

This section deals with the regime where the thermal boundary layer is much larger than the hydrodynamic boundary layer thickness. Practically liquid metals fall in this category. The radial velocity V_r scales as V_*. From the scaling of the differential form of continuity Eq. (5), the velocity scale in the axial direction is

$$V_z \sim \frac{\delta_T}{r_0} V_*. \tag{59}$$

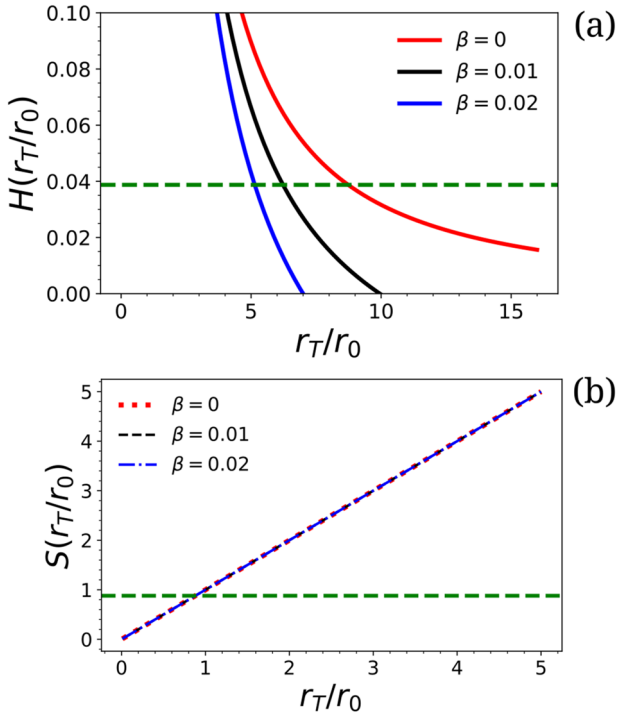

FIG. 9. (a) Graphical solution of r_T/r_0 for $\delta/\delta_T \gg 1$ with β as the parameter. (b) Graphical solution of r_T/r_0 for $\delta/\delta_T \ll 1$ with β as the parameter for $Re \sim 1000$.

Using the scales of V_r and V_z in Eq. (11), the scaling equivalent of the thermal energy equation becomes

$$\frac{V_*}{r_0}, \quad \frac{V_* \delta_T}{r_0 \delta_T} \sim \frac{\alpha}{\delta_T^2}. \tag{60}$$

Simplifying Eq. (60) and solving for the thermal boundary layer thickness, we have

$$\frac{\delta_T}{r_0} \sim Pe^{-1/2} Ro^{1/4} \left(\frac{V_\dagger}{V_*}\right)^{1/2}. \tag{61}$$

Using the scale of $V_* \sim V_0$ and using $V_\dagger / V_0 \sim Ro^{-1/2}$, Eq. (61) can be rewritten for $r < r_T$,

$$\frac{\delta_T}{r_0} \sim Pe^{-1/2} \sim Pr^{-1/2} Re^{-1/2}. \tag{62}$$

The Nusselt number scale for $r < r_T$ is, therefore, the reciprocal of Eq. (62),

$$Nu \sim Pr^{1/2} Re^{1/2}. \tag{63}$$

For $r > r_T$, the thermal boundary layer scales as the liquid film thickness as shown before in Eq. (22). The radial coordinate r_T is the distance from the central axis, where the thermal boundary layer meets the liquid film thickness profile. For $r > r_T$ the Nusselt number scales as

$$Nu \sim \left(\frac{r}{r_0}\right)\left(\frac{r_0}{h_0}\right)[E(r)]^{-1}. \tag{64}$$

Figure 8(d) depicts the Nusselt number as described by Eqs. (63) and (64) for $Re \sim 10\,000$, $Pr = 0.1$ and β as the parameter. The Nusselt number remains constant upto a critical radius r_T, beyond which the Nusselt number increases with radial coordinate. The evaporation is important at larger radial coordinate $r/r_0 > 2$. It can be further inferred from Fig. 8(d) that increased evaporation flux (means higher β) increases the Nusselt number. Note due to a very thin hydrodynamic boundary layer, the Nusselt number does not dependent on the Rossby number.

I. Scaling of r_T for $\delta/\delta_T \ll 1$

The scaling for r_T in this regime can be developed by equating the scales of thermal boundary layer height profile with liquid film thickness profile. Equating scales of Eq. (62) with Eq. (33), we have

$$\frac{r_T}{r_0} \frac{1}{E(r_T)} \sim Pr^{1/2} Re^{1/2} \left(\frac{h_0}{r_0}\right). \tag{65}$$

As before, we have solved Eq. (65) graphically for r_T/r_0. The solution is represented in Fig. 9(b). $S(r_T/r_0)$ represents a function of r_T/r_0 and β,

$$S(r_T/r_0) = \frac{r_T/r_0}{1 - \beta((r_T/r_0)^2 - 1)}. \tag{66}$$

Figure 9(b) represents an interesting feature that critical radius r_T in this regime is independent of evaporation flux. The critical value of r_T/r_0 is 0.9 for $Re \sim 1000$ and $Pr \sim 0.1$. The scaling laws for the thermal boundary layer are used to derive the average liquid jet temperature scale. The two different kinds of boundary conditions, isothermal plate and constant heat flux case, are discussed in the following sections.

J. Thin film average temperature for the isothermal plate

The liquid thin film average temperature can be evaluated by using the scales of thermal boundary layer thickness. Applying integral conservation of thermal energy across the CV (refer to Fig. 1),

$$\rho Q_{in} c_p T_i + \frac{k(T_0 - T(r))}{\delta_T(r)} \sim \rho V_r(r) 2\pi r h(r) c_p T(r) + j\pi(r^2 - r_0^2) h_{fg}, \tag{67}$$

where c_p is the specific heat capacity of the liquid, ρ is the density of the liquid, T_i is the temperature of the jet at the inlet entering the control volume, k is the thermal conductivity of the liquid, T_0 is the temperature of the rotating isothermal plate, $T(r)$ is the temperature of the liquid film averaged over the thermal boundary layer thickness, and h_{fg} is the latent heat of vaporization. From integral continuity Eq. (3), we have

$$r V_r(r) h(r) = \frac{1}{2\pi}\left[Q_{in} - \frac{j\pi(r^2 - r_0^2)}{\rho}\right]. \tag{68}$$

Substituting Eq. (68) in Eq. (67), the thermal energy balance equation scales as

$$\rho Q_{in} c_p T_i + \frac{k(T_0 - T(r))}{\delta_T(r)} \sim \rho c_p \left[Q_{in} - \frac{j\pi(r^2 - r_0^2)}{\rho}\right] T(r) + j\pi(r^2 - r_0^2) h_{fg}, \tag{69}$$

where $A = \rho Q_{in} c_p T_i$, $f(r) = \rho c_p [Q_{in} - \frac{j\pi(r^2 - r_0^2)}{\rho}]$, and $g(r) = j\pi(r^2 - r_0^2) h_{fg}$,

$$A + \frac{k(T_0 - T(r))}{\delta_T(r)} \sim f(r) T(r) + g(r). \tag{70}$$

The first term on the left-hand side A signifies the internal energy entering the control volume. The second term denotes the average heat flux entering the control volume from the heated rotating plate, while $f(r)$ and $g(r)$ are related to the effects of evaporative flux on the average liquid film temperature,

$$T(r)\left[f(r) + \frac{k}{\delta_T(r)}\right] \sim A + \frac{kT_0}{\delta_T(r)} - g(r), \tag{71}$$

$$T(r) \sim \frac{A + \frac{kT_0}{\delta_T(r)} - g(r)}{f(r) + \frac{k}{\delta_T(r)}}. \tag{72}$$

Most importantly, the average liquid film temperature scale depends on the temperature of the liquid jet entering the control volume and the thermal boundary layer thickness scale. Figure 10(a) shows the average temperature variation with a radial coordinate for different β

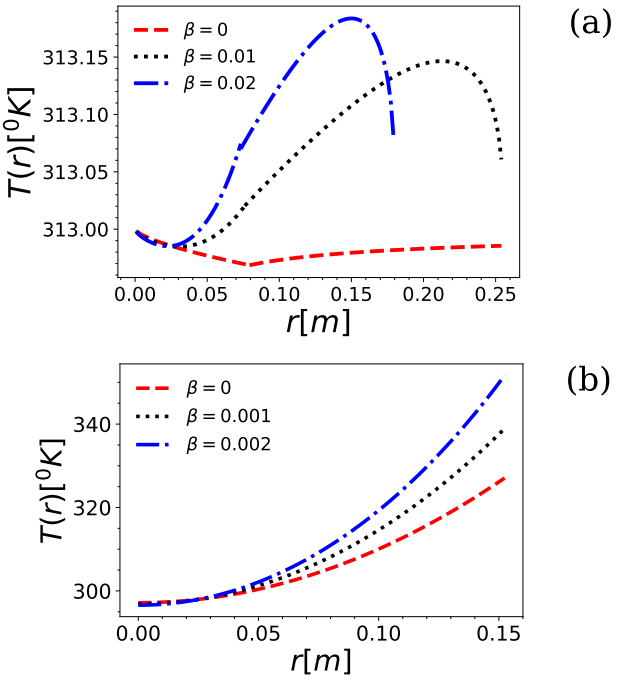

FIG. 10. (a) Average liquid film temperature as a function of the radial coordinate with β as the parameter for an isothermal plate. The plate temperature is at T_0 = 313 K, and the liquid inlet temperature entering the control volume is T_i = 298 K. (b) Average liquid film temperature as a function of the radial coordinate with β as the parameter for the constant heat flux case. The inlet temperature of the jet is T_i = 298 K, and the constant heat flux at the plate is $q'' = 2 \times 10^5$ W/m^2.

as described by Eq. (72). Increasing beta (evaporation flux) increases the average temperature field. The maximum temperature peak also shifts toward the left. Figure 9(a) is plotted for water with an inlet temperature of T_i = 298 K and a constant plate temperature of T_0 = 313 K.

K. Thin film average temperature for the constant heat flux case

Following a similar line of reasoning as for constant temperature conditions, the average liquid film temperature scale for constant heat flux is derived in this section. Applying integral conservation of thermal energy (refer to Fig. 1),

$$\rho Q_{in} c_p T_i + q''\pi(r^2 - r_0^2) \sim \rho V_r(r) 2\pi r h(r) c_p T(r) + j\pi(r^2 - r_0^2) h_{fg}, \tag{73}$$

where q'' is the constant heat flux at the surface of the rotating heated plate. Using integral continuity equation (3),

$$\rho Q_{in} c_p T_i + q''\pi(r^2 - r_0^2) \sim \rho c_p \left[Q_{in} - \frac{j\pi(r^2 - r_0^2)}{\rho} \right] T(r) + j\pi(r^2 - r_0^2) h_{fg}. \tag{74}$$

The average liquid film temperature scales as

$$T(r) \sim \frac{\rho Q_{in} c_p T_i + q''\pi(r^2 - r_0^2) - j\pi(r^2 - r_0^2) h_{fg}}{\rho c_p \left(Q_{in} - \frac{j\pi(r^2 - r_0^2)}{\rho} \right)}. \tag{75}$$

Comparing Eq. (72) with Eq. (75) shows the dependence of the average temperature field on the thermal boundary layer thickness scale for constant temperature boundary conditions. Furthermore, the average radial temperature field is directly proportional to the inlet temperature T_i, and the heat flux q'' as can be inferred from Eq. (75). The average liquid film temperature scale is plotted using Eq. (75) in Fig. 10(b). The effect of evaporation is understood by visualizing the dependence of the average temperature on β. The average temperature of the liquid film increases with the radial coordinate and increases with increasing evaporation flux. This is in accordance with the constant heat flux boundary conditions, where the average temperature increases monotonically with radial coordinate.

IV. CONCLUSION

We provided an integrodifferential scaling analysis to analyze the steady laminar free jet impacting a rotating hot plate. Integral mass conservation scaling in conjunction with the differential form of mass continuity, linear radial momentum, and boundary layer equations was used to capture the scales of the liquid film thickness and the hydrodynamic/thermal boundary layer thickness. Liquid film thickness, Nusselt number, and average thin-film temperature scalings and correlations were also derived. The analysis was carried out using pure scaling arguments without assuming any velocity or temperature distributions. The evaporative effects found were weak primarily as can be observed from equations having proper fractional indices for $E(r)$ (primarily, the indices for $E(r)$ were 1/3 and 1/9 in most cases). However, successive necessary corrections have to be considered for larger radial coordinates where evaporative effects are significant. The average liquid film temperature scale was then calculated using the thermal boundary layer profile and the integral form of the thermal energy equation. We compared the deduced scales with experimental data available in the literature. The experimental trends of liquid film thickness and Nusselt number on different non-dimensional numbers were in harmony with the scaling laws discovered.

AUTHOR DECLARATIONS

Conflict of Interest

The authors have no conflicts to disclose.

Author Contributions

Durbar Roy: Conceptualization (equal); Formal analysis (equal); Investigation (equal); Writing – original draft (equal); Writing – review & editing (equal). **Saptarshi Basu**: Conceptualization (equal); Formal analysis (equal); Methodology (equal); Supervision (equal); Writing – original draft (equal); Writing – review & editing (equal).

DATA AVAILABILITY

The data that support the findings of this study are available within the article.

REFERENCES

[1] T. Bohr, P. Dimon, and V. Putkaradze, "Shallow-water approach to the circular hydraulic jump," J. Fluid Mech. **254**, 635–648 (1993).
[2] B. W. Webb and C.-F. Ma, "Single-phase liquid jet impingement heat transfer," Adv. Heat Transfer **26**, 105–217 (1995).
[3] B. Ozar, B. M. Cetegen, and A. Faghri, "Experiments on heat transfer in a thin liquid film flowing over a rotating disk," J. Heat Transfer **126**, 184–192 (2004).
[4] J. Rice, A. Faghri, and B. M. Cetegen, "Analysis of a free surface film from a controlled liquid impinging jet over a rotating disk including conjugate effects, with and without evaporation," in *Heat Transfer Summer Conference*, 47322 (ASME, 2005), pp. 311–322.
[5] H. Schlichting, *Boundary Layer Theory* (McGraw Hill Book Co, New York, 1968).
[6] A. Aziz, "Hydrodynamic and thermal slip flow boundary layers over a flat plate with constant heat flux boundary condition," Commun. Nonlinear Sci. Numer. Simul. **15**, 573–580 (2010).
[7] D. Womac, S. Ramadhyani, and F. Incropera, "Correlating equations for impingement cooling of small heat sources with single circular liquid jets," J. Heat Transfer **115**, 106–115 (1993).
[8] K. A. Estes and I. Mudawar, "Comparison of two-phase electronic cooling using free jets and sprays," J. Electron. Packag. **117**, 323–332 (1995).
[9] C. Y. Y. Lee, M. L. Woyciekoski, and J. B. Copetti, "Experimental study of synthetic jets with rectangular orifice for electronic cooling," Exp. Therm. Fluid Sci. **78**, 242–248 (2016).
[10] A. Pavlova and M. Amitay, "Electronic cooling using synthetic jet impingement," J. Heat Transfer **128**, 897–907 (2006).
[11] S. Thomas, W. Hankey, A. Faghri, and T. Swanson, "One-dimensional analysis of the hydrodynamic and thermal characteristics of thin film flows including the hydraulic jump and rotation," J. Heat Transfer **112**, 728–735 (1990).
[12] E. J. Watson, "The radial spread of a liquid jet over a horizontal plane," J. Fluid Mech. **20**, 481–499 (1964).
[13] M. Rahman, A. Faghri, and W. Hankey, "Computation of turbulent flow in a thin liquid layer of fluid involving a hydraulic jump," J. Fluids Eng. **113**, 411 (1991).
[14] M. M. Rahman and A. Faghri, "Numerical simulation of fluid flow and heat transfer in a thin liquid film over a rotating disk," Int. J. Heat Mass Transfer **35**, 1441–1453 (1992).
[15] T. L. Labus, *Liquid Jet Impingement Normal to a Disk in Zero Gravity* (National Aeronautics and Space Administration, 1977), Vol. 1017.
[16] C. T. Avedisian and Z. Zhao, "The circular hydraulic jump in low gravity," Proc. R. Soc. London, Ser. A **456**, 2127–2151 (2000).
[17] X. Liu and J. Lienhard, "Liquid jet impingement heat transfer on a uniform flux surface," Heat Transfer Phenom. Radiat., Combust. Fires **106**, 523–530 (1989).
[18] A. Rao and J. H. Arakeri, "Integral analysis applied to radial film flows," Int. J. Heat Mass Transfer **41**, 2757–2767 (1998).
[19] S. Basu and B. Cetegen, "Analysis of hydrodynamics and heat transfer in a thin liquid film flowing over a rotating disk by the integral method," J. Heat Transfer **128**, 217 (2006).
[20] S. Basu and B. Cetegen, "Effect of hydraulic jump on hydrodynamics and heat transfer in a thin liquid film flowing over a rotating disk analyzed by integral method," J. Heat Transfer **129**, 657 (2007).
[21] T. Azuma and T. Hoshino, "The radial flow of a thin liquid film: 1st report, laminar-turbulent transition," Bull. JSME **27**, 2739–2746 (1984).
[22] Z. H. Chaudhury, "Heat transfer in a radial liquid jet," J. Fluid Mech. **20**, 501–511 (1964).
[23] X. S. Wang, Z. Dagan, and L. M. Jiji, "Heat transfer between a circular free impinging jet and a solid surface with non-uniform wall temperature or wall heat flux—1. Solution for the stagnation region," Int. J. Heat Mass Transfer **32**, 1351–1360 (1989).
[24] H. Carper, Jr. and D. Deffenbaugh, "Heat transfer from a rotating disk with liquid jet impingement," in *International Heat Transfer Conference Digital Library* (Begel House Inc., 1978).
[25] H. Carper, Jr., J. Saavedra, and T. Suwanprateep, "Liquid jet impingement cooling of a rotating disk," J. Heat Transfer **108**, 540 (1986).
[26] R. Fernandez-Feria, E. Sanmiguel-Rojas, and E. S. Benilov, "On the origin and structure of a stationary circular hydraulic jump," Phys. Fluids **31**, 072104 (2019).
[27] B. Mohajer and R. Li, "Circular hydraulic jump on finite surfaces with capillary limit," Phys. Fluids **27**, 117102 (2015).
[28] B. Scheichl, "Centred splash of a vertical jet on a horizontal rotating disc: Recent findings and resolving controversies over the hydraulic jump," in *Boundary and Interior Layers, Computational and Asymptotic Methods BAIL* (Springer, 2020), pp. 201–213.
[29] U. Sen, S. Chatterjee, J. Crockett, R. Ganguly, L. Yu, and C. M. Megaridis, "Orthogonal liquid-jet impingement on wettability-patterned impermeable substrates," Phys. Rev. Fluids **4**, 014002 (2019).
[30] E. S. Benilov, "Hydraulic jumps in a shallow flow down a slightly inclined substrate," J. Fluid Mech. **782**, 5–24 (2015).
[31] Y. Wang and R. E. Khayat, "Impinging jet flow and hydraulic jump on a rotating disk," J. Fluid Mech. **839**, 525–560 (2018).
[32] Y. Wang and R. E. Khayat, "The influence of heating on liquid jet spreading and hydraulic jump," J. Fluid Mech. **883**, A59 (2020).
[33] R. K. Bhagat, N. Jha, P. Linden, and D. I. Wilson, "On the origin of the circular hydraulic jump in a thin liquid film," J. Fluid Mech. **851**, R5 (2018).
[34] A. Duchesne, A. Andersen, and T. Bohr, "Surface tension and the origin of the circular hydraulic jump in a thin liquid film," Phys. Rev. Fluids **4**, 084001 (2019).
[35] A. Duchesne, L. Lebon, and L. Limat, "Constant Froude number in a circular hydraulic jump and its implication on the jump radius selection," Europhys. Lett. **107**, 54002 (2014).
[36] R. K. Bhagat and P. F. Linden, "The circular capillary jump," J. Fluid Mech. **896** (2020).
[37] L. Landau and E. Lifshitz, Fluid Mechanics: Theoretical Physics (Butterworth-Heinemann, 1987), Vol. 6.
[38] C. K. Batchelor and G. Batchelor, *An Introduction to Fluid Dynamics* (Cambridge University Press, 2000).
[39] P. K. Kundu, I. M. Cohen, and D. Dowling, *Fluid Mechanics*, 4th ed. (Elsevier Science, 2008).
[40] A. Bejan, *Convection Heat Transfer* (John Wiley & Sons, 2013).
[41] S. Sankaran, B. Ozar, B. Cetegen, and A. Faghri, "Experiments on heat transfer in a thin liquid film flowing over a rotating disk," Trans. ASME **126**, 184–192 (2004).